Increased Strength in Wind Turbine Blades through Innovative Structural Design[*]

J. A. Paquette[†]
Sandia National Laboratories[‡]
japaque@sandia.gov

P. S. Veers[†]
Sandia National Laboratories[‡]
psveers@sandia.gov

Abstract:

When a system design approach is applied to wind turbine blades, manufacturing and structural requirements are included along with aerodynamic considerations in the design optimization. The resulting system-driven design includes several innovative structural features such as flat-back airfoils, a constant thickness carbon spar-cap, and a thin, large diameter root. Subscale blades were manufactured to evaluate the as-built integrated performance. The design resulted in a 22% reduction in mass, but withstood over 300% of its design load during testing. Compressive strains of nearly 0.9% were measured in the carbon spar-cap. The test results from this and an earlier design are compared, as are finite element models of each design. Included in the analysis is a review of the acoustic emission events that were detected through the use of surface mounted microphones.

Keywords: wind turbine blade, structural testing, acoustic emissions, flat-back airfoils, carbon fiber

1 Introduction

When a system design approach is applied to wind turbine blades, manufacturing and structural requirements are included along with aerodynamic considerations in the design optimization. The resulting system-driven design includes several innovative structural features that might not even be considered if only aerodynamic performance were under consideration. For example, the manufacturing process is greatly simplified and product quality is enhanced if the structural spar cap can remain constant thickness over a majority of the blade span. Rather than go the expense of new molds for multi-megawatt scale blades, approximately 9m long subscale blades were manufactured to evaluate the as-built performance of the design innovations.

While three blade designs were constructed and evaluated in this program (including a passive twist-coupled blade) the demonstration of the integrated design depends on only two of the designs, so the detailed discussions of test results is limited to the blades that demonstrate the features of the system-driven blade design. Although a twist-coupled blade was built, tested, and met its design criteria, it is not discussed further in this work.

1.1 Blade Research Program at Sandia National Laboratories

In 2002, Sandia National Laboratories initiated a research program to demonstrate the use of carbon fiber in subscale blades and to investigate advanced structural concepts through the Blade System Design Study (BSDS). From this effort, three 9 m designs were created by Sandia with assistance from Global Energy Concepts, Dynamic Design, and Mike D. Zuteck Consulting; seven blades from each design were manufactured by TPI Composites of Warren, Rhode Island. Three blades were for structural testing, three for field testing and one was a spare.

1.2 Blade Designs

The first blade set was called CX-100 (Carbon Experimental), and contained a full-length carbon spar cap, a relatively new concept at the time. The geometry of the CX-100 is a classical representation of blades of the 9m scale where the aerodynamic design is prescribed before the structural design is specified. It was based on the design of the ERS-100 blade [1] at outboard span stations, with a slightly modified root diameter.
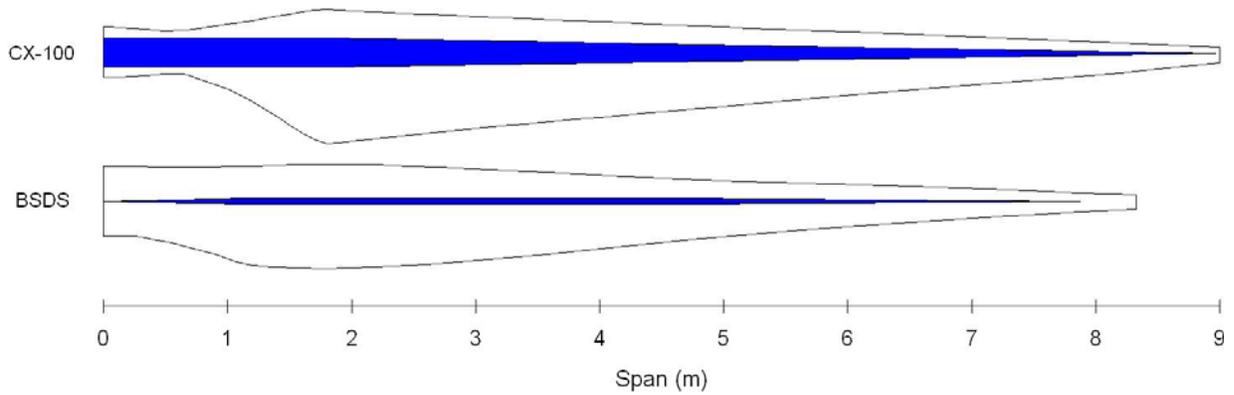
Figure 2: CX-100 (top) and BSDS (bottom) blade plan forms and carbon regions (blue).
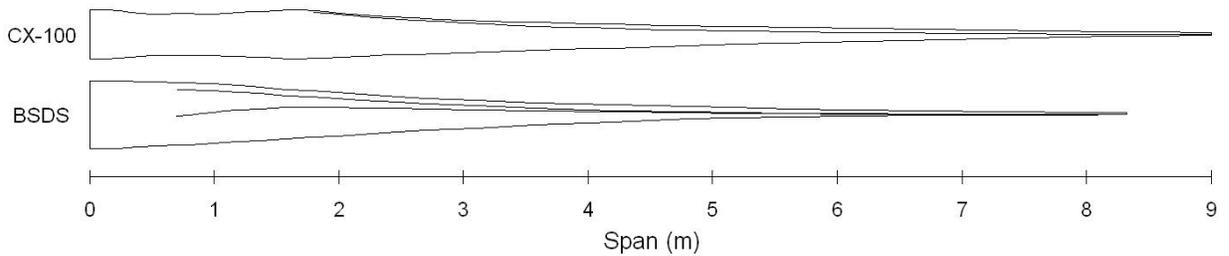
Figure 1: CX-100 (top) and BSDS (bottom) blade geometries as viewed from the trailing edge.

The second blade design was named the BSDS, owing its name to the research program under which it was created – the Blade System Design Studies. The BSDS had a length of 8.325 m rather than the 9.00 m length of the CX-100. This blade design exhibited a highly efficient structure which included such features as a thin, large-diameter root; flat-back airfoils; integrated root studs; and a full-length, constant-thickness, carbon spar cap. A drawing of the plan forms of these blades is shown in Figure 2, with the carbon-containing areas shown in blue. Note the carbon spar caps of the CX-100 and the BSDS blades. The narrow, constant thickness spar cap of the BSDS blade is enabled by the inherent structural stiffness of this design. In addition, the BSDS design features a gradual transition between the root and max-chord areas as compared to the CX plan form. Figure 1 provides a view of the two different blade geometries as seen from the trailing edge. Note the flat-back on the inboard portion of the BSDS blade, as well as the larger root and smoother chord thickness transition.

Figure 3 shows the airfoil geometries and relative sizes at the root, max-chord, and tip of the CX-100 and BSDS blades. Note that in the figure the airfoils are shown without pre-twist. The BSDS blade can be seen to have a larger root diameter while also having a shorter max-chord length. The tip airfoil of the BSDS blade is representative of the outboard

airfoils in the blade which are thin and aerodynamically high performing.
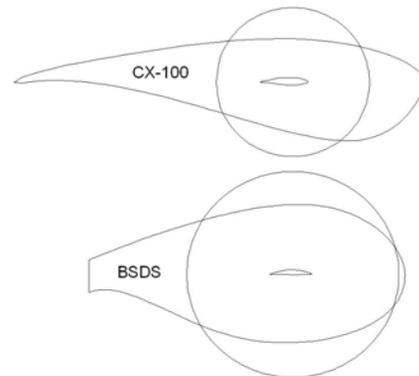
Figure 3: 9 m airfoil geometries at root, max-chord, and tip

The design innovations of the BSDS blade were made possible by a system design approach. In this way, the design of the system – aerodynamics, structure, and manufacturing – are optimized collectively rather than letting one design consideration control the others. The end result is a compromise by all parties in the design process which requires extensive communication and design iteration. The system design approach led the designers of the BSDS to adopt flat-back airfoils for the inboard portion of the blade. These airfoils are produced by opening up the trailing edge of the blade

uniformly along the camber line. Thus, these airfoils are different than truncated airfoils in that they preserve the camber of the original airfoil. Flatback airfoils allow for increased thickness without some of the disadvantages associated with conventional thick airfoils. Varying the thickness of the airfoil without a resulting change in the chord length allows for a better solution for both the structural designer and the manufacturer. Figure 4 shows the thickness distribution along the span of the BSDS blade as compared to that of the CX-100 blade. The flat-back airfoils can be seen to allow for a thicker cross-section in the inboard portion of the blade where loads are highest.
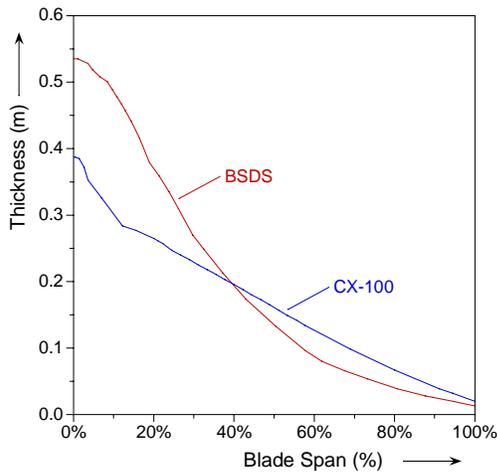
Figure 4: Airfoil thicknesses vs. span for CX-100 and BSDS.

In addition to structural advantages, flat-back airfoils produce more lift than conventional airfoils. This allows for shorter chord lengths which is important for transportation issues on utility-scale blades. Also, flat-back airfoils have less sensitivity to soiling as compared to conventional airfoils.

These benefits do not come without risks, however, as there may be issues associated with aeroacoustics, excess drag, and three-dimensional flow along the trailing edge. It is believed that the issue of noise emanating from the flat-back airfoils should be mitigated by their inboard location where airspeeds are low along with the observation that noise increases with the fourth or fifth power of incident airspeed. Three-dimensional airflow uncertainties and drag have not been fully modeled. However, trailing edge devices such as splitter plates have shown promise in alleviating these issues.

The intention of this work is to summarize the evaluation of the structural strength testing and compare the results to the finite element model predictions of strain and deflection. This comparison

offers some insight into the capabilities of the finite element models to predict static test performance. Buckling analyses are also presented to provide insight into the ability to predict failure loads.

2 Testing

A suite of laboratory and field tests were proposed to verify that the manufactured blades met their design goals. In the laboratory, the blades were to undergo modal, static, and fatigue testing. To date, specimens from each design have undergone modal and static testing. This paper will focus on results from the static testing.

2.1 Test Setup

A CX-100 and a BSDS blade were tested to static failure at the National Wind Technology Center (NWTC) near Boulder, CO. The blades were mounted to a 1360 kN-m test stand and subjected to a flapwise bending load to approximate the extreme loading case for the design wind class. The CX-100 blade was designed for an extreme load case that resulted in a root moment of 86.4 kN-m [2] while the extreme root moment for the BSDS blade was 53.8 kN-m [3]. The blades were loaded with a three-point whiffle-tree and saddle arrangement which was connected to an overhead bridge crane. The apparatus is shown schematically in Figure 5. The saddle locations and applied test loads are given in Table 1.
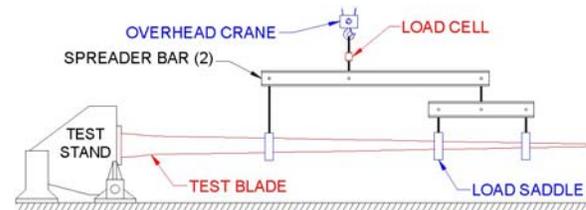
Figure 5: Three point whiffle-tree used in 9 m static blade tests.

Saddle #	CX-100		BSDS	
	Position (m)	Load (kN)	Position (m)	Load (kN)
1	3.00	16.91	3.00	9.79
2	5.81	5.47	4.80	3.96
3	7.26	5.59	6.60	3.65

*Loads are for 100% test load

Table 1: Saddle positions and loads* for CX-100 and BSDS static blade tests.

The blades were loaded and unloaded in increasing 25% increments of the test load until the test load was reached as shown in Figure 6. At each load step, the load was held for approximately 60 s. The 100% test load was calculated by multiplying the design

load distribution by a safety factor of 1.10. The resulting distribution was then approximated with a piece-wise linear fit achieved by the point loads applied at the saddle locations. The desired and applied test moment distributions for the CX-100 and BSDS blade tests are shown in Figure 7. After reaching the 100% test load, loads were increased in 10% increments and held for 60 s until failure occurred (see Figure 6).
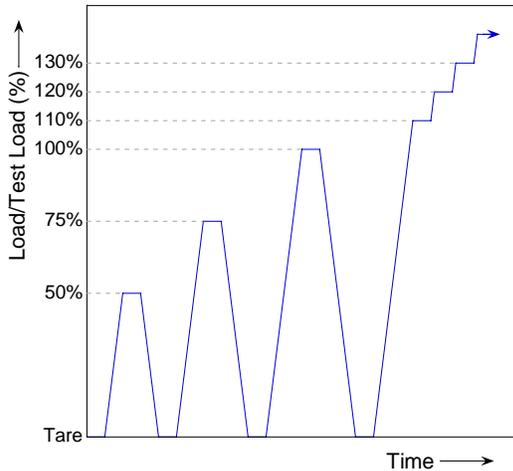
Figure 6: Loading sequence for 9 m blade tests.
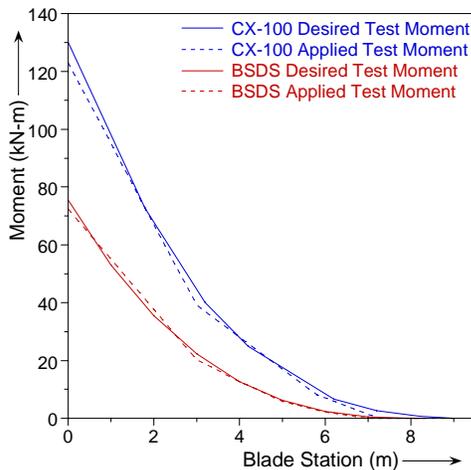
Figure 7: CX-100 and BSDS test loading distribution.

Strain, deflection, load, and acoustic emissions were recorded throughout the tests. Load was monitored with a 100 kN load cell mounted between the whiffle-tree and the overhead crane (see Figure 5). Deflection was measured by three string potentiometers attached along the trailing edge near the saddle positions. The test blades were outfitted with a suite of 30-40 strain gages to measure strains along the blade centerline, in large panel regions near

max-chord, and at other material and structural points of interest. Finally, the blades were instrumented with a grid of surface-mounted PAC R6I sensors to detect acoustic events.

2.2 Test Results

Each test blade successfully withstood its prescribed test load. The CX-100 blade failed at a root moment of 128.6 kN-m [4] while the BSDS blade failed at root moment of 203.9 kN-m [5].

Figure 8 shows the maximum deflections that were measured in the three blade tests along with their corresponding root moments. The deflection curves were calculated through a polynomial fit of the string pot results. The maximum calculated tip deflections for the CX-100 and BSDS blades were 1.05 m and 2.79 m respectively. Additionally, Figure 8 compares the deflections of both blades at a root moment of 100 kN-m. The results show that the CX-100 blade was significantly stiffer than the BSDS blade.
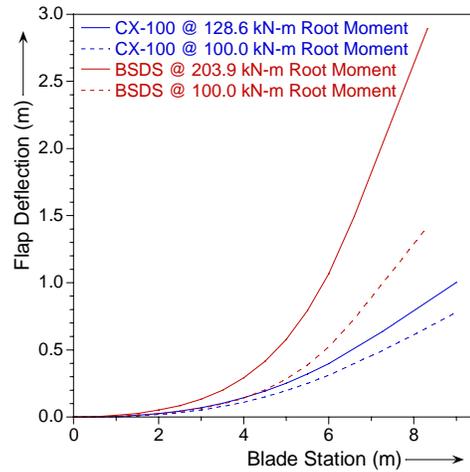
Figure 8: CX-100 and BSDS measured deflections.

Figure 9 shows the maximum strains measured along the high-pressure and low-pressure spar caps for the CX-100 and BSDS blades just before failure. The carbon spar cap of the CX-100 blade experienced maximum strains of around 3000 µε in both tension and compression before failure. The carbon spar cap of the BSDS blade experienced maximum strains of over 8000 µε in both tension and compression.

Figure 10 and Figure 11 give the strains measured in the buckling-prone panel regions aft of the spar cap for the CX-100 and BSDS blades. Nonlinearities in the strain response indicate a change in the load path and can be associated with the emergence of a structural instability. The CX-100 blade showed indications of buckling in the 1.800 m region near a root moment of about 117 kN-m. The

BSDS blade showed slight signs of buckling at the 1.575 m station at around a 150 kN-m root moment.
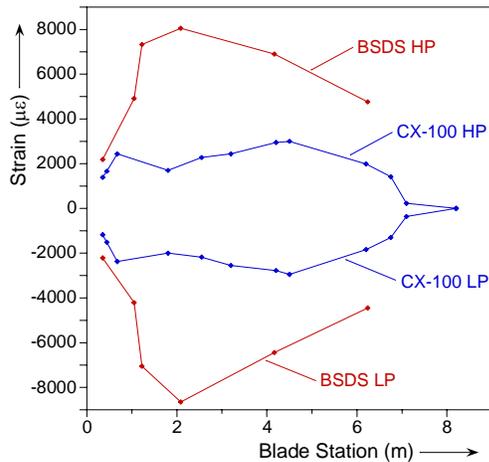
Figure 9: CX-100 and BSDS measured spar cap strains near the failure load.
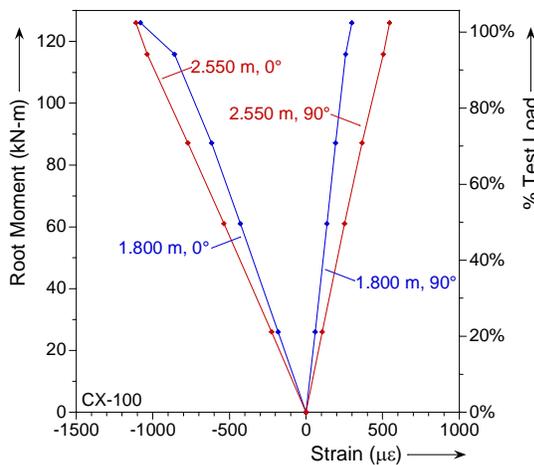
Figure 10: CX-100 measured aft panel strains parallel (0°) and perpendicular (90°) to blade axis.

Strain gages were placed on the flat-back of the BSDS, perpendicular to the blade axis, at 0.580 m and at 1.575 m. The 0.580 m station contained one gage in the middle of the flat-back (labeled 50%). At the 1.575 m station, gages were placed on the high pressure surface near the edge of the flat-back (labeled 0%), on the low pressure surface near the flat-back (labeled 100%), and on the flat-back at two intermediate positions, 25% and 75% of the distance between the high-pressure and low-pressure surfaces. The gages were intended to indicate if the flat-back was warping or rotating relative to the high-pressure and low-pressure surfaces during the test. Figure 12 shows the strains measured at the aforementioned locations. Strain was linear with respect to load at the 0.580 m location, suggesting that the flat-back was

not warped inward or outward at this location. All gages at the 1.575 m location show evidence of changes in the load path, especially beyond a root moment of 150 kN-m. The 0% and 25% gages start to change from compression to tension while the 75% and 100% begin to change from tension to compression. This suggests that the flat-back was beginning to warp by the low-pressure edge caving in. The strains changing in opposite directions at the opposite ends of the flat-back suggest that the flat-back was not experiencing a uniform concave or convex panel buckling at the 1.575 m location.
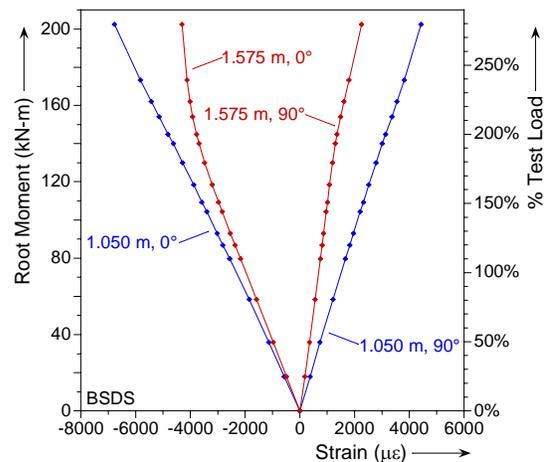
Figure 11: BSDS measured aft panel strains parallel (0°) and perpendicular (90°) to blade axis.
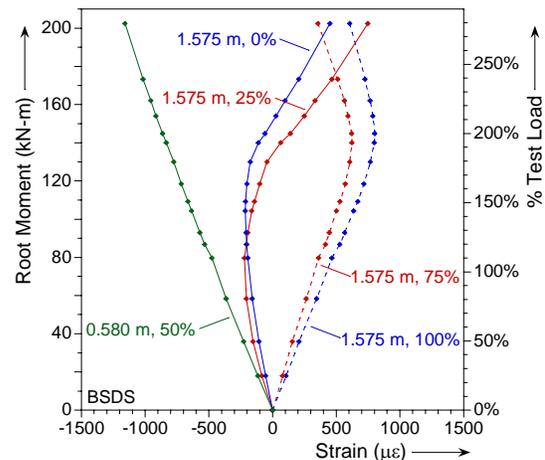
Figure 12: BSDS measured flat-back strains.

Acoustic emissions caused by fiber breakage or matrix cracking can be used to indicate the location of local damage in the blade. This is accomplished by deploying an array of microphones on the surface and setting a time window in which individual microphones can sense the same event. The difference in time at which the event is detected by

each microphone is used to triangulate the position on the surface that the microphones are mounted, assuming the velocity profile of the substrate is known. Unfortunately, the velocity profile is complicated in a composite structure which contains materials with directionally dependent acoustic transmission properties. The end result is a structure which has a velocity profile that depends on both location and direction. The various fits of the acoustic velocity field were used in this test – all of them with the form

$$v = a + b\left(\left|\cos\alpha\right|\right)^n \qquad (1)$$

where a, b, and n are fitting constants and α is the angle between the direction vector from the sensor to the event and the blade pitch axis. Higher order fits can be used, but this fitting scheme produced estimated accuracies of approximately 10 cm.

The event locations for the CX-100 and BSDS blade tests are shown in Figure 13 and Figure 14 respectively. Each event is color coded with a respective energy range. It should be noted that this energy metric is not the true energy, as it represents the integral of the voltage vs. time curve, rather than voltage squared. These voltage vs. time results are useful for comparative purposes however. The events are overlaid on outlines of each blade. Since the locations of the acoustic events are two-dimensional, the outlines are of the flattened low-pressure skins of the blades. Important material and structural regions of the blades are also shown.
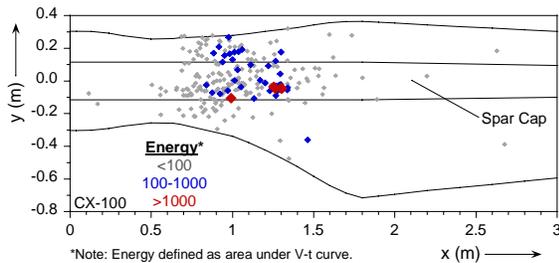
Figure 13: Measured acoustic event locations and energies for CX-100 blade test.
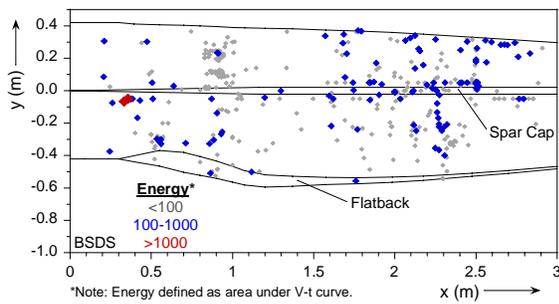
Figure 14: Measured acoustic event locations and energies for BSDS blade test.

Several high-energy events were located between 1.20 m and 1.30 m along the spar cap, above the shear web of CX-100 blade. The CX-100 blade was observed to experience a catastrophic buckling of the low-pressure skin near the 1.200 m station. A post mortem inspection of the blade in this region showed a large crack in the bond joint between the low pressure skin and the shear web. A photograph of the crack is shown in Figure 15.

The only high-energy events detected during the BSDS test were located around 0.350 m, which is where the shear web terminates on the root end. A closer examination of this area after the test showed that a large crack had developed between the low-pressure skin and the shear web in the bonding joint. A photograph of the crack is shown in Figure 16.

Figure 15: Crack in shear web to LP skin bond joint at 1.20-1.30 m on the CX-100 blade.
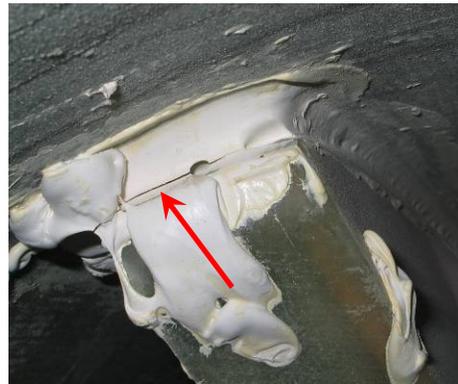
Figure 16: Crack at shear web termination on the LP surface of the BSDS blade.

During the initial static test of the BSDS blade, the blade catastrophically failed near the 5.00 m station, at a root moment of 203.9 kN-m. The complete catastrophic failure at this station prohibited the assessment of the mode of failure. This is interesting because panel buckling in the max chord region of the blade was not the limiting factor in the static

strength, which is usually the case for other blades of this size.

A second static strength test was performed on the remaining portion of the BSDS in an attempt to obtain a failure closer to the root. Load was applied by a two-point whiffle-tree with the distribution matched as closely as possible to the first test. During this second test, the blade failed near the 2.00 m station at a root bending moment of 220.2 kN-m.

Acoustic emission monitoring is also a valuable tool for assessing when failure is occurring locally or globally. Figure 17 and Figure 18 show the sum of the acoustic emission energy detected by all of the sensors in the root region of the CX-100 and BSDS blades. In each plot a trend line is drawn through the initial linear portions of the response. At some load, the response begins to become non-linear, indicating an acceleration of the acoustic emissions and thus internal damage. For the CX-100 blade, the acoustic emissions accelerate rapidly beyond root moments of 125 kN-m. The response from the BSDS blade remained mostly linear until a root moment of 140 kN-m was reached. The accumulation of acoustic energy in the BSDS blade did grow non-linearly after 140 kN-m, although not as rapidly as for the CX-100 blade.

Figure 18: BSDS measured acoustic energy accumulation.

Results of the CX-100 and BSDS static tests are summarized in Table 2. The relatively high strength of the BSDS blade is evident, with the measured carbon strains approaching values seen in coupon testing of some pre-preg specimens. This high strength, combined with the significantly lower weight, points to the structural advantages of this design in comparison to the CX-100.

Property	CX-100	BSDS
Weight (lb)	383	289
% of Design Load at Failure	115%	310%
Root Failure Moment (kN-m)	128.6	203.9
Max. Carbon Tensile Strain at Failure (%)	0.31%	0.81%
Max. Carbon Compressive Strain at Failure (%)	0.30%	0.87%
Maximum Tip Displacement (m)	1.05	2.79

Table 2: Summary of results of CX-100 and BSDS blade tests.

Figure 17: CX-100 measured acoustic energy accumulation.

3 Modeling

While the BSDS blade was designed with extensive use of the ANSYS/NuMAD finite element tool, the CX-100 design was mostly based on local section analysis. After the blades were built, both designs were analyzed with comprehensive finite element models to evaluate the structural performance, including modal frequencies, strain distributions and buckling loads. However, the comparison of these models with the static test results also offers the opportunity to evaluate the accuracy of finite element tools for design-strength calculations.

3.1 Model Development

Finite element models of the CX-100 and BSDS blades were generated in ANSYS using the NuMAD preprocessor. The models consisted of SHELL99 elements with an offset-node formulation used for the blade skins and a conventional mid-node formulation used for the shear web. It is generally preferable to use the offset-node formulation for blade skins as the outer surface is both defined and continuous whereas the mid-thickness plane is not. However, the offset-node formulation has been shown to have difficulties handling shear deformations [6]. A cross-section of the CX-100 model is shown in Figure 19. In this figure, the element thicknesses have been displayed as have the various laminate regions which are shown in different colors. Flanges and adhesive joints were not included in the models as they are not currently produced by the NuMAD pre-processor.
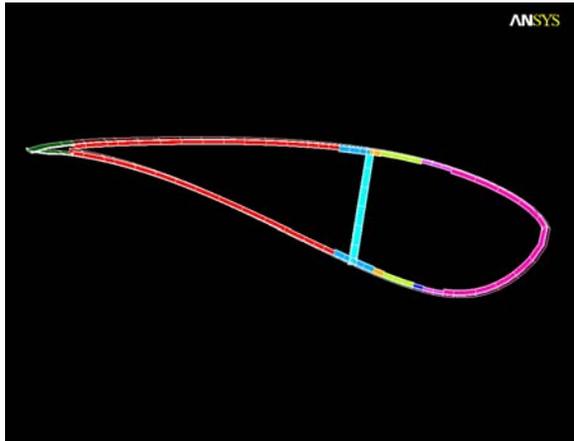
Figure 19: Cross-section of CX-100 finite element model.

The CX-100 model contained 13,659 elements while the BSDS model had 19,400 elements. The finite element models of the CX-100 and BSDS blades along with the loads and boundary conditions (cantilevered at the root) which were applied to them are shown in Figure 20 and Figure 21. In the figures, the different colors again represent the various laminate regions

Loads simulating the static tests were applied to the models by using a distribution of nodal point loads along the high-pressure surface at each of the saddle locations (see Figure 20, Figure 21, and Table 1). The point loads at each saddle location were made to be as similar as possible while applying the correct force, and with zero moment about the pitch axis. The nodes at the root end of the blade models were held fixed for the simulations.

The analyses that were used to compare to the test results assumed static loading with small displacements. An additional analysis was performed on each blade model to determine the linear buckling load and deformed shape.
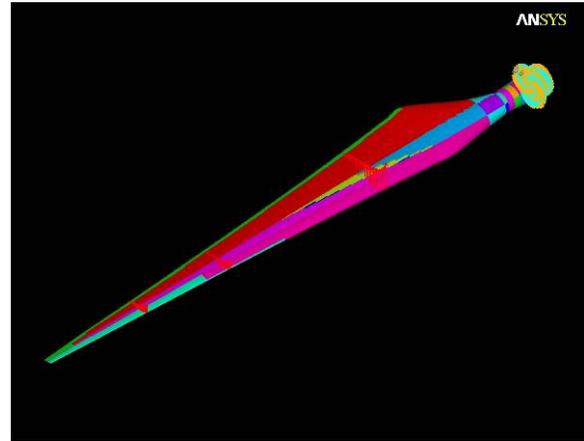
Figure 20: CX-100 finite element model.
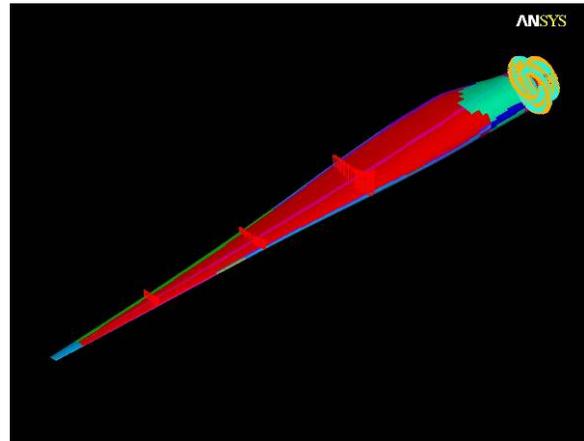
Figure 21: BSDS finite element model.

3.2 Modeling Results

The flap deflections given by the model are compared to the test results for a root moment of 100 kN-m in Figure 22. The CX-100 model slightly over predicted the flap displacements outboard of 7 m while the BSDS model is seen to have produced a closer match. Possible causes for error in the models include uncertainties in as-built material properties and geometries as well as slight differences in loading angles during the progression of the static tests.

Strains were measured along the high-pressure and low-pressure carbon spar caps during the tests. Figure 23 and Figure 24 compare the measured strains at a root moment of 100 kN-m to those obtained from the finite element analysis of the CX-100 and BSDS blades respectively. The CX-100 model over predicted the strains in the spar cap from

the 3–6 m span. This may indicate an error in the material properties, or could possibly be due to the omission of the shear-web flange that runs underneath the spar cap. The BSDS model compares more favorably with the test results except for some small discrepancies in the 2 m span area.
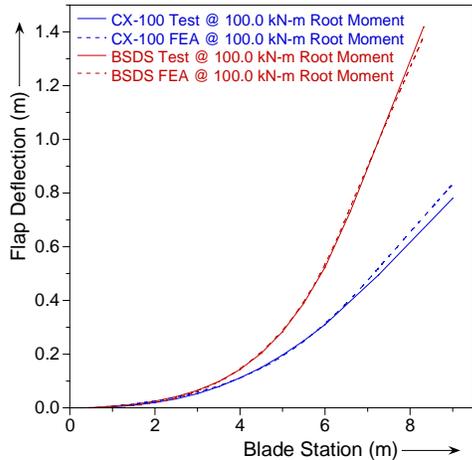
Figure 22: CX-100 and BSDS measured and FEA flap deflections.
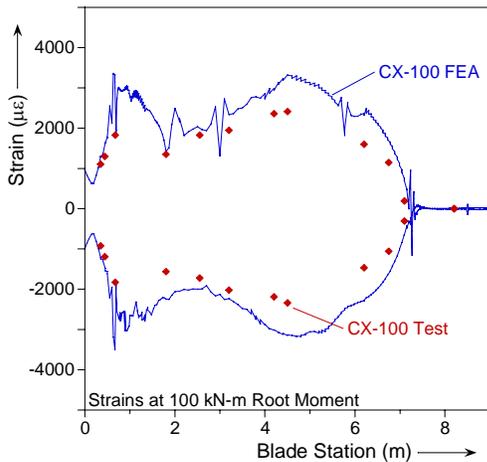
Figure 23: CX-100 measured and FEA spar cap strains.

The design of the BSDS blade has a smoother transition from the root region to the max-chord region. To examine the effect that this had on structural performance, the calculated strain fields were studied. Figure 25 shows the von Mises strain in the transition region of the CX-100 blade. The figure displays the rapidly changing strains as the blade transitions from the root section to the max-chord section. Figure 26 shows the same plot for the BSDS blade. In this figure, the strains are much more consistent throughout the transition region with the

exception of some strain concentrations along the spar cap outboard of max-chord location.
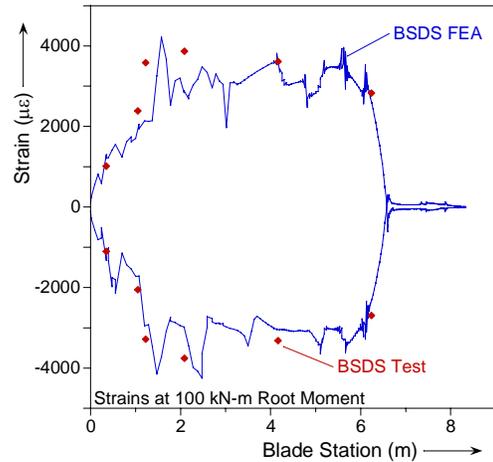
Figure 24: BSDS measured and FEA spar cap strains.
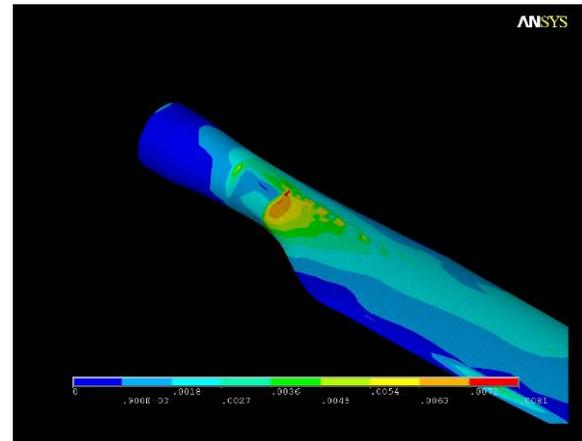
Figure 25: CX-100 transition region FEA strains.
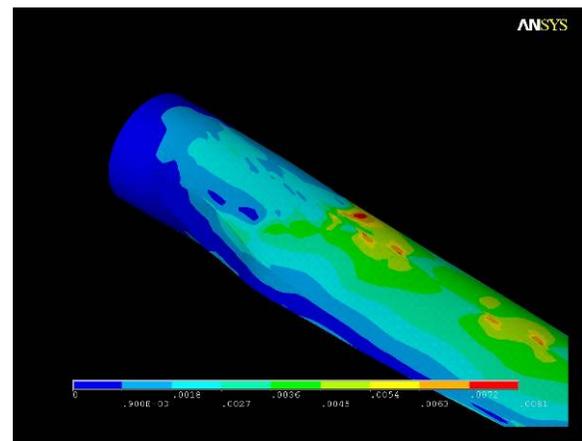
Figure 26: BSDS transition region FEA strains.

It should be stressed that linear buckling calculations are generally non-conservative due to the lack of as-

built imperfections in the model. In addition, buckling analyses of complex structures often produce a multitude of buckling modes with load levels that are similar. Therefore, the calculated buckled configurations represent likely scenarios where the deformation occurs away from boundary conditions such as load introduction points. The CX-100 blade model predicted a linear buckling load of 172 kN-m near the root. The predicted buckled configuration for the CX-100 is shown in Figure 27. The deformation is concentrated in the transition region between the root build-up and max-chord.
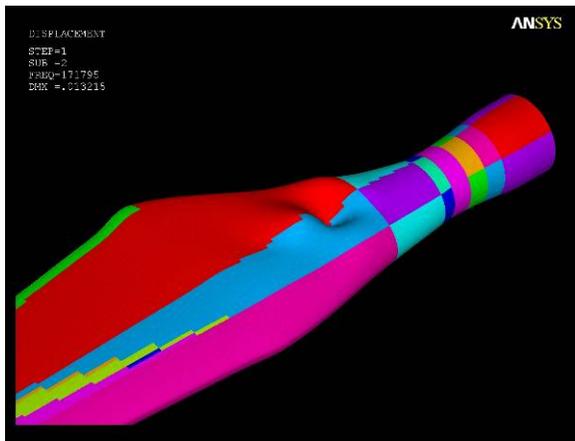
Figure 27: CX-100 linear FEA buckled shape.

The BSDS blade model predicted a linear buckling load of 200 kN-m at the root. The predicted buckled configuration for this blade is shown in Figure 28. Similar to the CX-100 model, the deformation is concentrated in the transition region between the root build-up and max-chord.
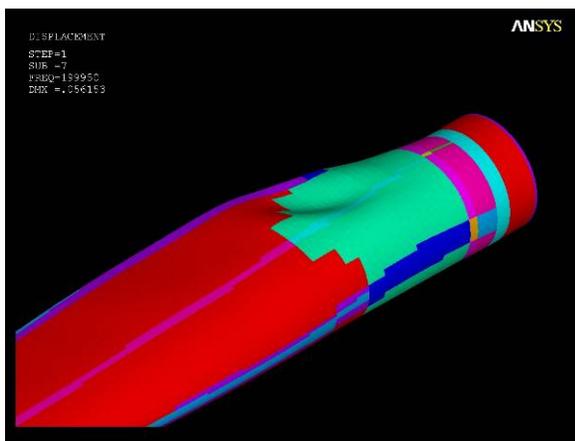
Figure 28: BSDS linear FEA buckled shape.

Conclusion

The structural advantages of the BSDS blade design has been demonstrated through static testing and modeling. Features such as a thin, large diameter root, shorter flat-back airfoils in the max-chord region, and a constant-thickness carbon spar cap resulted in a blade that was lighter and stronger than a conventional blade, which also contained a carbon spar cap. The structure of the BSDS blade also resulted in a much narrower spar cap than what was needed in the CX-100 blade. These structural innovations, while implemented in subscale blades, are applicable megawatt scale blades as well. The benefits are blades that can be both lighter and stronger at the same time while using less of the more expensive carbon fiber than more conventional blade designs. The aerodynamic performance, while estimated to be within a percent or two of conventional designs [3] is yet to be evaluated in field tests.

References

[1]. TPI Composites, Inc. Final Project Report, *Blade Manufacturing Improvements Development of the ERS-100 Blade*, SAND2001-1381, May 2001.

[2]. D. Berry, *Design of 9-meter Carbon-Fiberglass Prototype Blades Final Project Report*, SAND Report in preparation, Sandia National Laboratories, Albuquerque, NM, 2007.

[3]. D. Berry, *BSDSII Final Project Report*, SAND Report in preparation, Sandia National Laboratories, Albuquerque, NM, 2007.

[4]. J. Paquette, *Static Structural Testing of a CX-100 9m Wind Turbine Blade*, SAND Report in preparation, Sandia National Laboratories, Albuquerque, NM, 2007.

[5]. J. Paquette, *Static Structural Testing of a BSDS Wind Turbine Blade*, SAND Report in preparation, Sandia National Laboratories, Albuquerque, NM, 2007.

[6]. D. Laird, F. Montoya, and D. Malcolm, *Finite Element Modeling of Wind Turbine Blades*, ASME/AIAA Wind Energy Symposium, Reno, NV, 2005, pp. 9-17.